Int. J. Electrochem. Sci., 7 **(2012)** 6436 - 6452

International Journal of
ELECTROCHEMICAL
SCIENCE
www.electrochemsci.org

The Effects of Microstructure and Ag_3Sn and Cu_6Sn_5 Intermetallics on the Electrochemical Behavior of Sn-Ag and Sn-Cu Solder Alloys

Wislei R. Osório[1,2,*], *Leandro C. Peixoto*[2], *Leonardo R. Garcia*[2], *Amauri Garcia*[2], *José E. Spinelli*[3]

[1] School of Applied Sciences / FCA, University of Campinas, UNICAMP, Campus Limeira, 1300, Pedro Zaccaria St., Jd. Sta Luiza, 13484-350 Limeira, SP, Brazil
[2] Department of Materials Engineering, University of Campinas, UNICAMP, P.O. Box 6122, 13083–970 Campinas, SP, Brazil
[3] Department of Materials Engineering, Federal University of São Carlos, UFSCar, 13565-905 São Carlos, SP, Brazil
[*]E-mail: wislei@fem.unicamp.br

Received: 13 December 2011 / *Accepted:* 23 January 2012 / *Published:* 1 July 2012

The aim of this study is to evaluate the electrochemical corrosion behavior of Sn-2 wt.% Ag and Sn-2.8 wt.% Cu solder alloys in a 0.5 M NaCl solution at 25°C as a function of microstructure features and Ag_3Sn and Cu_6Sn_5 intermetallics. Both Sn-Ag and Sn–Cu alloys are becoming interesting lead-free solder alternatives. Microstructure morphologies obtained from a vertical water-cooled unidirectional solidification system under a cooling rate of about 15 °C/s are analyzed. Electrochemical impedance spectroscopy (EIS) diagrams, potentiodynamic polarization curves and an equivalent circuit analysis were used to evaluate the electrochemical parameters. It was found that although the relative cost 1.5 times higher for the Sn-2Ag alloy compared to that of the Sn-2.8Cu alloy, its corresponding electrochemical behavior is better in terms of polarization resistance, current density and pitting corrosion. This is shown to be intimately associated with the resulting fine and homogeneously distributed Ag_3Sn intermetallic particles in the Sn-rich matrix.

Keywords: solder alloys; solidification; intermetallics; corrosion, microstructure array

1. INTRODUCTION

The increasingly environmental concern over the toxicity of Pb combined with strict regulations, are gradually banning the use of lead-based solders providing an inevitable driving force for the development of lead-free solder alloys [1-5]. A number of binary alloys have been examined as candidates for replacement of the traditional Sn-Pb solder alloy, such as Sn-Ag and Sn-Cu alloys. High

wettability, high electrical and thermal conductivities, low thermal expansion coefficient, good mechanical strength, ductility, creep resistance, thermal fatigue resistance and manufacturability besides a low cost are desirable characteristics required for solder alloys.

The Sn-Ag solder alloy can be considered as a promising candidate due to their compatible properties with the Sn–Pb solder [6-7]. Typical hypoeutectic Sn-Ag alloys have as-cast microstructures formed by a Sn-rich dendritic matrix and a eutectic mixture of a Sn-rich phase and intermetallic Ag_3Sn particles located in the interdendritic regions. These Ag_3Sn intermetallic particles can considerably accelerate the dissolution of tin from the solder matrix into the corrosive medium due to galvanic corrosion mechanisms [8]. High cooling rates during soldering are associated with spheroid-like Ag_3Sn particles while very low cooling rates are related to the formation of Ag_3Sn particles which are characterized by a mixture of plate-like and fiber-like morphologies [9-12]. It is also known that the Ag content of the alloy can strongly affect the morphology of Ag_3Sn particles [9-11]. It is also known that the Ag_3Sn intermetallic has an important role on the resulting mechanical behavior of solder joints. Brittle Ag_3Sn particles may lead to serious problems under stressed conditions of service for printed wiring boards [11].

Considering the Sn-Cu alloys, it can be said that they are becoming an interesting lead-free solder alternative, mainly due to cost issues and the facility to be transferred to practical production [13-14]. Sn-Cu solder alloys have a eutectic reaction at 227°C that occurs between the faceted intermetallic Cu_6Sn_5 phase and the non-faceted Sn-rich phase [6; 14].

Although both the Sn-Cu and Sn-Ag alloys can be considered as promising solder alternatives, few studies highlighting the effects of the morphologies and scales of the phases constituting their microstructures on the corresponding electrochemical corrosion behavior can be found in the literature [6-7, 9-10, 15]. Li et al. [8] using a potentiodynamic polarization analysis have demonstrated that a Sn-3.5Ag alloy has better corrosion resistance than Sn-Ag-Cu and Sn-Cu solder alloys in a 3.5% NaCl solution. The corrosion of solder alloys is not generally a major problem. However, in many applications the solder alloy is directly exposed to air moisture, mixture of air and industrial pollutants (e.g. sulphur ions) and oceanic environments (sodium chloride ions) [8]. Li et al. [8] have also stated that the most used electronic packaging method, i.e. wire bonding and flip chip package, makes the solders to be exposed directly to corrosion media, such as underfill materials, air, moisture, air pollutants from industry and oceanic environments, depending on their application. In order to have a high reliability, solder materials must be resistant to such corrosion agents.

It would be interesting to correlate the morphologies of the intermetallic Ag_3Sn and Cu_6Sn_5 particles connected to the morphology and scale of the Sn-rich matrix, with the influent parameters during the cooling stage of the soldering process. That would permit to attain guidelines with a view to preprogramming a desired performance in terms of the required final properties of solder joints, based on the microstructural arrangement. In this context, the present study aims to elucidate the role of fine microstructure arrays of both Sn-2 wt.% Ag and a Sn-2.8 wt.% Cu solder alloys, which are formed under high cooling rates (of about 15 ^{o}C/s, typical of soldering operations), on the resulting electrochemical corrosion behavior in a 0.5 M NaCl solution at 25 ^{o}C

2. EXPERIMENTAL PROCEDURE

2.1 Specimens preparation

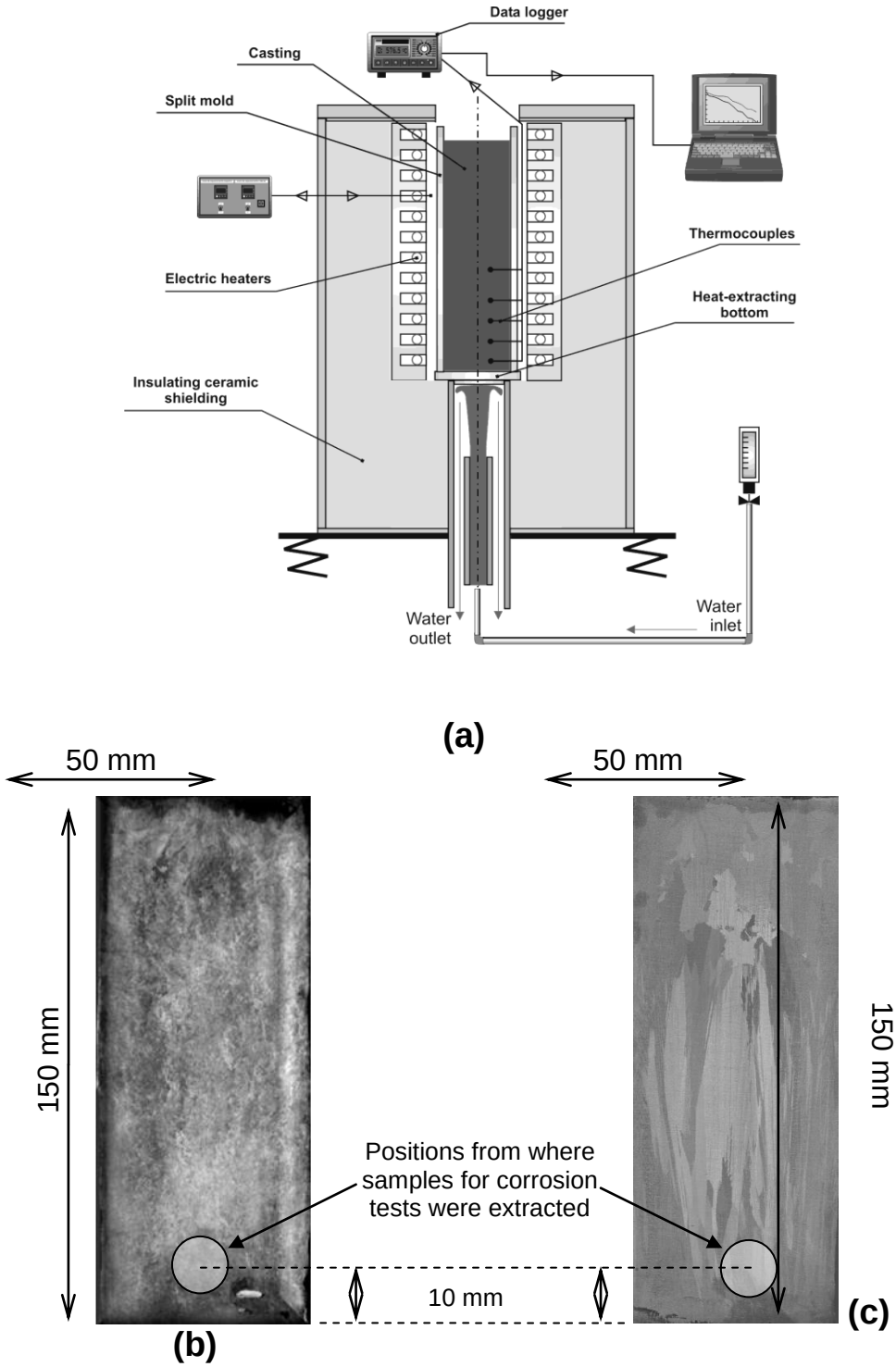

Figure 1. (a) Schematic representation of the experimental solidification set-up where: 1) computer and data acquisition software; 2) insulating ceramic shielding; 3) electric heaters; 4) mold; 5) thermocouples; 6) data logger; 7) heat-extracting bottom; 8) water flow meter; 9) temperature controller; 10) casting, and (b) Longitudinal equiaxed and (c) columnar macrostructures of the Sn-2.8%Cu and Sn-2%Ag alloys, respectively.

Commercially pure grade (c.p.) Sn (99.993 wt.%) and Cu (99.991 wt.%) were used to prepare the Sn-2.8 wt.% Cu alloy. The mean impurities detected were: Fe (0.001%), Si (0.002%), Zn (0.004%), and Pb (0.002%), Fe (0.007%), respectively, besides other elements found with concentrations less than 100 ppm. Considering the Sn-2 wt.% Ag alloy, the used c.p. grades were: Sn (99.991wt.%) and Ag (99.993wt.%), and the corresponding mean impurities detected were: Fe (0.001wt.%), Si (0.002wt.%), Cu (0.005wt.%), and Sn (0.002wt.%), Pb (0.0045 wt.%), respectively, besides other minor elements with concentration less than 50 ppm.

Two directionally solidified castings of both Sn-2.8%Cu and Sn-2%Ag alloys were obtained by using a water-cooled unidirectional solidification apparatus, which was designed in such way that the heat is extracted only through the water-cooled bottom, promoting vertical upward directional solidification, as shown in Fig. 1(a).

Samples for microstructural characterization and corrosion tests were extracted from a position in the castings at about 10 mm from the cooled bottom (at longitudinal sections), as shown in Fig. 1b and 1c. These samples were further ground using silicon carbide papers up to 1200 mesh, polished and etched to reveal the microstructure (etching solution of 92% vol. CH_3OH, 5% vol. HNO_3 and 3% vol. HCl applied for 5s). The castings were sectioned along the longitudinal direction and the macrostructure was revealed (2 mL HCl; 10g $FeCl_3$ and 100 mL H2O).

Microstructural characterization was performed using an optical microscope associated with an image analysis system Olympus GX51 (Olympus Co., Japan) and a Field Emission Gun (FEG) - Scanning Electron Microscope (SEM) Philips (XL30 FEG) coupled to an Energy Dispersive Spectroscope -EDS (Oxford Link ISIS 300). X-ray diffraction (XRD) measurements were carried out in order to determine the constitution of the phases forming the samples microstructure. XRD patterns were obtained utilizing a XRD-7000 Shimadzu with a 2-theta range from 20° to 100°, Cu-Kα radiation with a wavelength, λ, of 0.15406 nm. The segregation samples were underwent a fluorescence spectrometer, model Shimadzu EDX-720 to estimate their average concentration through an area of 100 mm^2 probe.

Continuous temperature measurements in the casting were monitored during solidification via the output of a bank of fine type J thermocouples sheathed in 1.6 mm outside diameter (O.D.) stainless steel tubes.

2.2 Corrosion tests

The working electrodes (Sn-Ag and Sn-Cu alloys samples) were positioned at the glass corrosion cell kit, leaving a circular 1.0 (±0.02) cm^2 metal surface in contact with a naturally aerated and stagnant 500 cm^3 of a 0.5 M NaCl solution at 25^oC having a pH of 7(±0.5). The samples were further carefully ground to a 1200 grit SiC finish, followed by distilled water washing and air drying before electrochemical measurements. EIS measurements began after an initial delay of 15 minutes for the sample to reach a steady-state condition. A potentiostat (EG & G Princeton Applied Research, model 273A) coupled to a frequency analyzer system (Solartron model 1250), a glass corrosion cell kit with a platinum counter-electrode and a saturated calomel reference electrode (SCE) were used to

perform the EIS tests. The potential amplitude was set to 10 mV; peak-to-peak (AC signal) in open-circuit, with 5 and 6 points per decade and the frequency range was set from 100 mHz to 100 kHz. Each EIS test was carried out for about 20 minutes. Immediately after the EIS tests, the potentiodynamic polarization tests were carried out for about 40 to 50 minutes.

Potentiodynamic tests were also carried out in a 0.5 M NaCl solution at 25^{o}C using a potentiostat at the same positions and immediately after the EIS measurements. These tests were conducted by stepping the potential at a scan rate of 0.1667 mVs^{-1} from -250/+250 mV (SCE) at open-circuit. Using an automatic data acquisition system, the potentiodynamic polarization curves were plotted and both corrosion rate and potential were estimated by Tafel plots using both anodic and cathodic branches. Duplicate tests for both EIS and potentiodynamic polarization curves were carried out. In order to supply quantitative support for discussions of these experimental EIS results, a model (ZView® version 2.1b) for equivalent circuit quantification has also been used.

3. RESULTS AND DISCUSSION

3.1 Macro and Microstructures

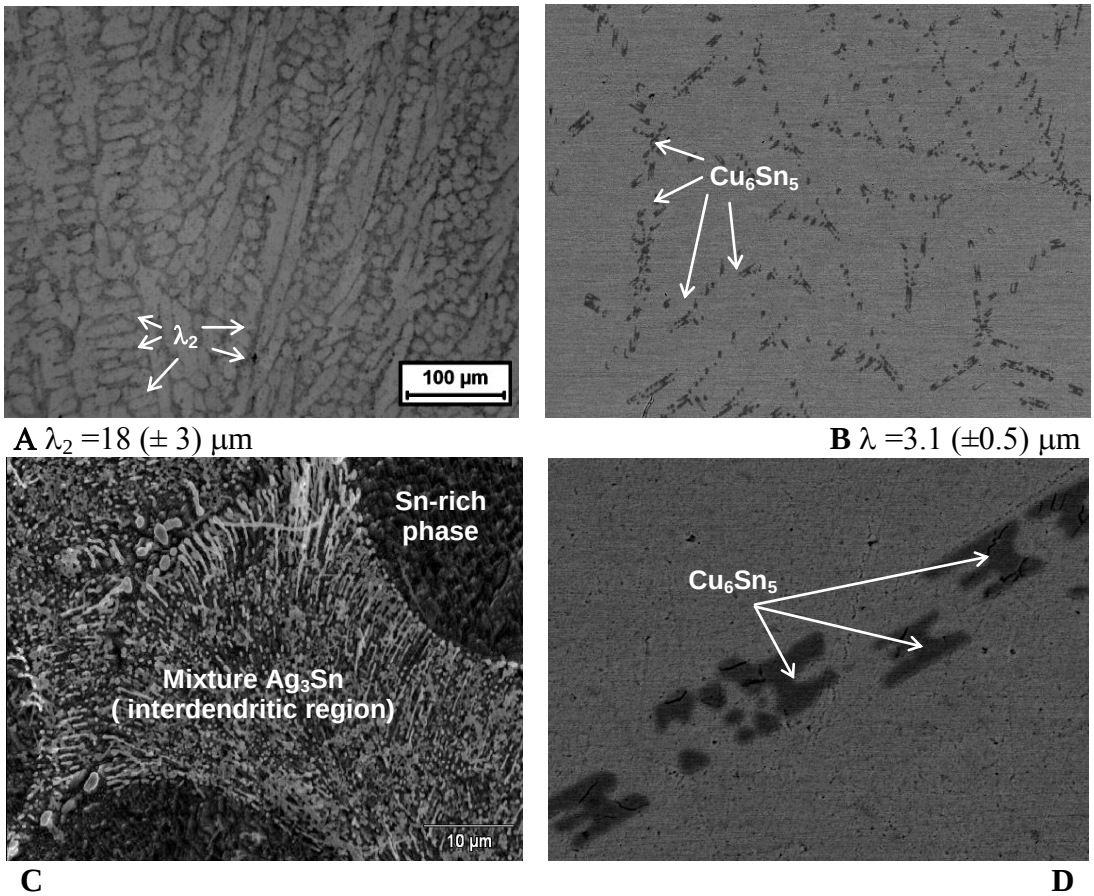

A λ_2 =18 (± 3) µm **B** λ =3.1 (±0.5) µm

C **D**

Figure 2. Typical micrographs of **(a)** Sn-2% Ag and **(b)** Sn-2.8% Cu solder alloys cooled at high cooling rates and SEM images at higher magnifications evidencing **(c)** Ag_3Sn and **(d)** Cu_6Sn_5 intermetallics.

The macrostructures of the Sn-2%Ag and Sn-2.8%Cu alloys were characterized by columnar grains and equiaxed grains along the castings lengths, respectively, as shown in Fig. 1(b) and (c). It is important to remark that the cooling rates are higher close to the cooled bottom decreasing along the casting length towards the top of the casting, as previously reported [4-5; 9-10; 14]. The examined samples were extracted from a region close to the casting surface, as shown in Fig. 1(b) and 1(c), where the solidification cooling rates are considered to be similar to those applied during most soldering procedures. In this sense, the resulting microstructures can also be considered similar to those which result from soldering processes with these alloys compositions.

Considering the microstructure of the Sn-Ag solder alloy, the Ag_3Sn particles are characterized by a mixture of spheroids and fiber-like morphologies when a high cooling rate (± 12 $^oC/s$) is applied during solidification. As shown in Fig. 2 (a) and (c), the resulting microstructure is formed by a matrix of Sn-rich phase, which is a solid solution of Ag in Sn (of about 0.05 wt.% Ag) with a eutectic mixture (± 3.5 wt.% Ag) in the interdendritic region (light region in Fig. 2 (c)). Fine secondary dendrite arm spacings (λ_2 = 12 μm) characterize the Sn-rich matrix (light regions in Fig. 2(a)). The eutectic mixture is constituted by a cooperative growth of Ag_3Sn intermetallics (± 73 wt.% Ag) and the Sn-rich phase (± 0.05 wt.% Ag). In previous investigations [9-10], it was verified that microstructures of a Sn-2 wt.% Ag alloy having a coarse dendritic array (± λ_2 = 80 μm), combined with a mixture of fiber-like and plate-like Ag_3Sn intermetallic particles provided deleterious effects on the corrosion resistance. This coarse microstructure was associated with a cooling rate of about 0.02 $^oC/s$ during solidification [9-10].

The microstructure of the Sn-Cu solder alloy sample is constituted by a Sn-rich matrix (α: solid solution of Cu in Sn) and Cu_6Sn_5 intermetallic particles randomly distributed in the Sn-rich matrix.

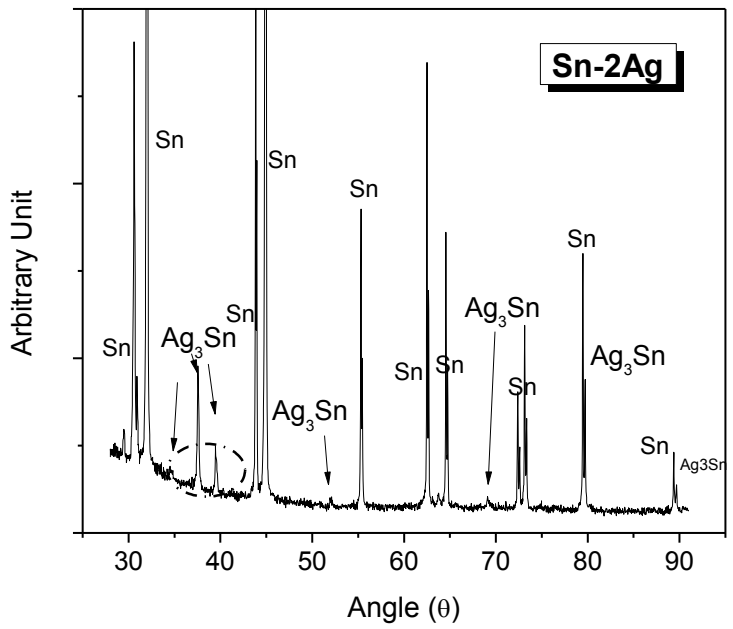

A

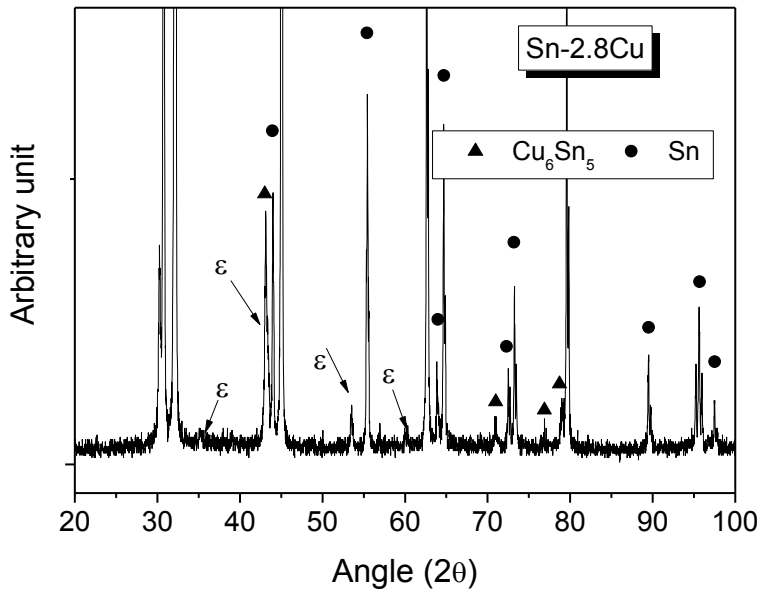

B

Figure 3. Typical X-ray diffraction patterns of Sn-2%Ag and Sn-2.8%Cu solder alloys samples.

As shown in Fig. 2 (b) and (d), the light regions are Sn-rich areas and dark regions are intermetallic particles, which are commonly called H-shaped [16] or M-shaped [17] Sn-Cu intermetallics, [14, 16-17]. The average inter-brach spacing (λ) of the intermetallic particles was shown to be 3.1 (±0.5) μm for a cooling rate of about 15 ^{o}C/s during solidification.

Fig. 3 exhibits the resulting XRD patterns for both Sn-Ag and Sn-Cu solder alloys samples. Peaks are associated with the Sn-rich phase for both cases, with presence of Ag_3Sn and Cu_6Sn_5 intermetallics for the Sn-Ag and Sn-Cu alloys, respectively. Correlating these XRD plots with the corresponding microstructure shown in Fig. 2(a) and (c), it can be said that Ag_3Sn is constituted by a mixture of spheroids with fiber-like particles. Fig. 3(a) evidences these peaks, which have been mainly detected at 37.5, 39.5, 52 and 69 degrees, as similarly reported in previous investigations [9-10; 18-19].

Considering the Sn-Cu solder alloy sample and correlating the XRD diagram with the resulting microstructure shown in Fig. 2 (b) and (d), it can be seen that both Cu_3Sn (ε phase) and Cu_6Sn_5 phases have been detected. These latter intermetallics are normally found in SnCu or Sn-based alloys solder joints containing Cu, and can be mainly associated with the final properties of the welded assembly [18-19]. On the other hand, the ε phase is particularly detected when high cooing rates are applied [20-21].

3.2 EIS plots and equivalent circuit

Fig. 4 (a) depicts the Bode and Bode-phase plots representing the modulus of impedance (/Z/) and phase angle (θ) as a function of frequency (F). The examined Bode and Bode-phase plots

indicate similar corrosion kinetics for both Sn-Ag and Sn-Cu solder alloys evidencing one time constant.

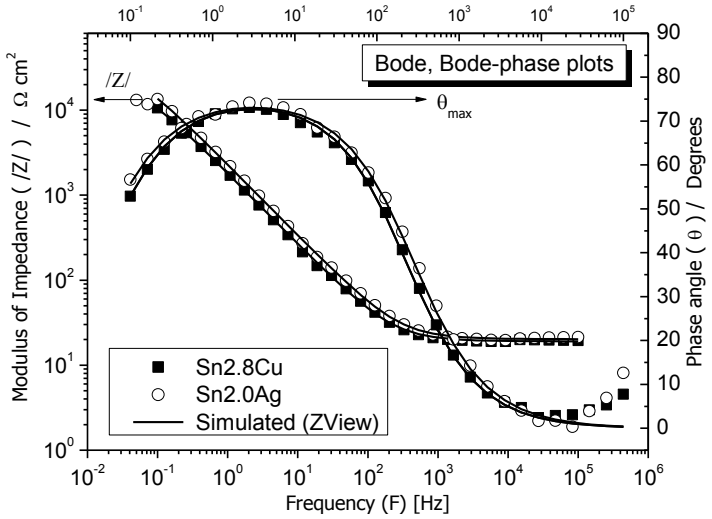

A

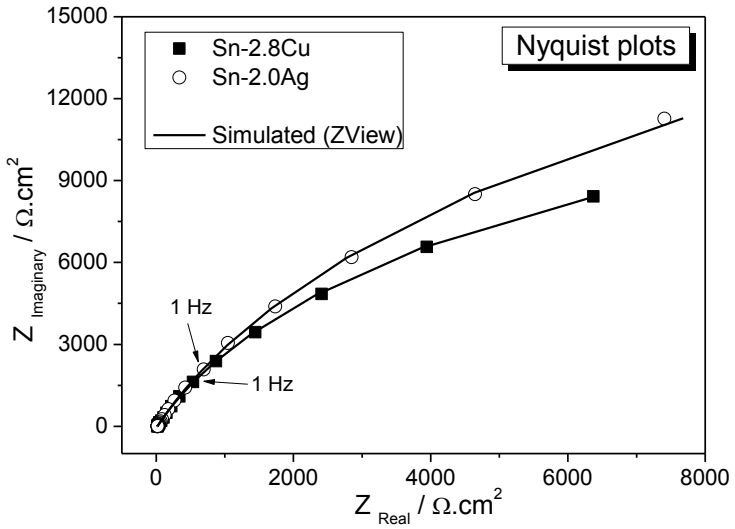

B

Figure 4. (a) Experimental Bode and Bode-Phase representations and **(b)** Nyquist plots of the Sn-2%Ag and the Sn-2.8%Cu solder alloys samples.

At frequencies ranging between 10^3 to 10^5 Hz, reactions between the electrolyte and the sample are characterized. At low frequencies (between 0.1 and 10 Hz), the time constant seems to be related to the reaction with the Sn-rich matrix. At a frequency of 0.1 Hz, very similar /Z/ values of about 10^4 Ω cm^2 are clearly observed. It can also be observed similar maximum phase angles ($\theta_{max.}$) of about 75° with a frequency of 3 (±1) Hz. The Bode and Bode-phase plots for both Sn-Ag and Sn-Cu solder alloys samples examined, do not allow significant differences to be observed. However, slightly different capacitive semi-arcs are shown in Nyquist plots, as depicted in Fig. 4(b). This difference is only

evidenced for frequencies lower than 1 Hz which correspond to high Z_{Real} and $Z_{Imaginary}$ semi-arcs (e.g. from 1000 Ω cm^2 and 3000 Ω cm^2). This observation gives indications that the Sn-2Ag alloy sample has a slightly better electrochemical behavior than the Sn-2.8Cu alloy when these fine microstructures (obtained at a cooling rate of about 15 ^{o}C/s) are compared. However, only these experimental (qualitative) results of EIS are not enough to guarantee that Ag additions to Sn increase the corrosion resistance when compared with similar Cu additions. In this sense, it would be interesting to analyze the impedance parameters which can be obtained by the ZView® software. The interpretation of the physical elements of the proposed *Rel (Z_{CPE}R1)* equivalent circuit will permit both the charge transfer resistance and the capacitance associated with the polarization resistance to be better understood.

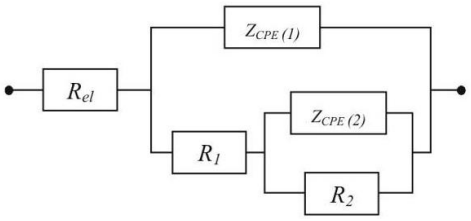

Figure 5. Proposed equivalent circuit used to obtain impedance parameters.

Table 1. Impedance parameters of a Sn-2.0 wt.% Ag and a Sn-2.8 wt.% Cu solder alloys samples.

Parameters	SnAg	SnCu
R_{el} (Ω cm^2)	20.2	19.06
Z_{CPE} (μFcm^{-2})	92.5 (±5)*	110 (±4)*
n	0.84	0.84
R_1 (kΩ cm^2)	39.2 (±4.1)*	26.3 (±1.8)*
χ^2	12.5 10^{-3}	6.4 10^{-4}

(*) Values into the parenthesis are errors resulting from fitting the experimental data in the equivalent circuit analysis

Fig. 5 shows the proposed single equivalent circuit used to fit the experimental data. Table 1 shows the impedance parameters obtained by the ZView® software and the chi-squared (χ^2) values which were used to evaluate the fitting quality. The physical elements of the proposed equivalent circuit are: R_{el} which is the electrolyte (solution) resistance, R_1 is the charge transfer resistance, which can be associated with the oxide (product of corrosion) film resistance and Z_{CPE} is the constant-phase element for products of corrosion film and represents the capacitance associated with the polarization resistance R_1 [9-10, 14, 22-32]. The parameter "n" is related to the phase angle, varying between -1 and 1. The impedance of a constant phase element is defined as $Z_{CPE} = [C\ (j\omega)^{n}]^{-1}$ where "C" is the capacitance; "j" is the current; "ω is the frequency and $-1 \leq n \leq 1$ [22-32].

Considering the measured impedance parameters, mainly those associated with the polarization resistances (R_1), it can be inferred that both the microstructure arrangement and the type of solute (Ag or Cu) have important roles on the electrochemical behavior of the Sn-2% Ag and Sn-2.8%Cu alloys.

Despite the similar capacitance results (Z_{CPE}), the Sn-Ag solder alloy has R_1 (polarization resistance) of about 1.5 times higher than that of the Sn-Cu alloy sample. This indicates a better electrochemical corrosion resistance connected with the Sn-Ag alloy. However, it would be interesting to analyze the potentiodynamic polarization curves and their corresponding parameters, such as the corrosion current density, corrosion potential and pitting potential.

3.3 Polarization measurements

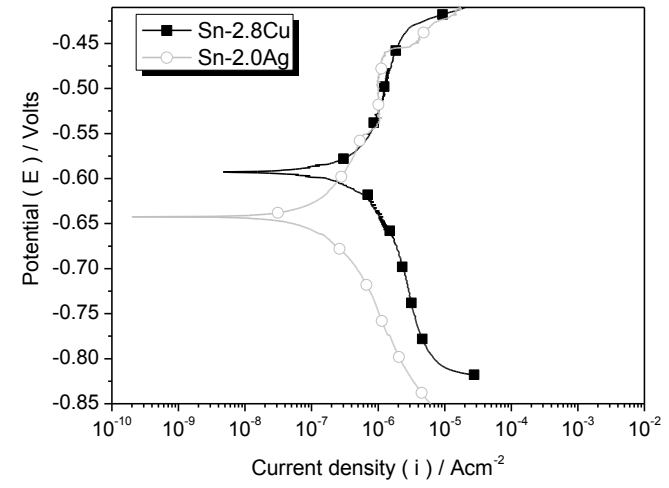

A

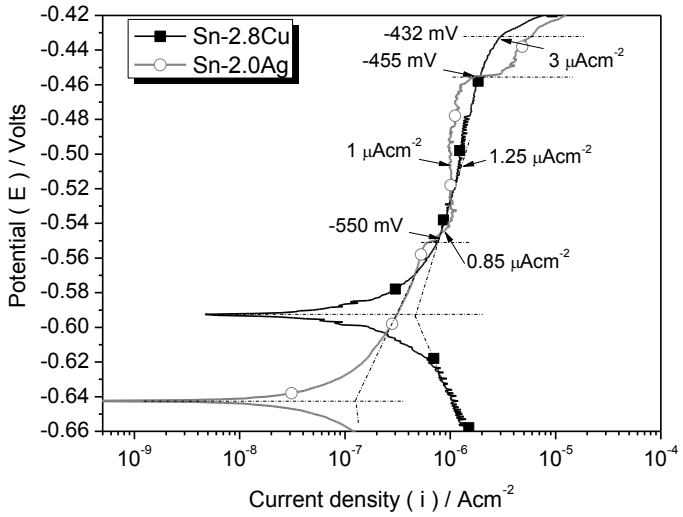

B

Figure 6. **(a)** Experimental potentiodynamic polarization curves and **(b)** detail evidencing pitting potentials and primary passive current for both Sn-2%Ag and Sn-2.8%Cu solder alloys samples in a 0.5 M NaCl solution at 25 ^{o}C.

The potentiodynamic polarization curves experimentally determined will be used to confirm the trends which have been previously observed with experimental and simulated EIS results. Fig. 6(a)

shows the anodic and cathodic branches of potentiodynamic polarization curves (from -850 mV to -410 mV, SCE) for both the Sn-Ag and Sn-Cu solder alloy samples carried out in a stagnant and naturally aerated 0.5 M NaCl solution at 25^{o}C.

Details of the anodic branches (from -660 mV to -420mV, SCE) of these curves permit the pitting potential (E_{pit}) to be evaluated, as shown in Fig. 6(b). These results reinforce the corrosion resistance tendency observed previously with the results of EIS and impedance parameters (equivalent circuit). The corrosion current density (i_{corr}) was obtained by Tafel extrapolation considering both the cathodic and anodic branches (from -680 mV to -540 mV, SCE) of the polarization curves, as shown in Fig.7. It is important to remark that the use of very small scan rates is suggested in order to minimize the effects of distortion in Tafel slopes and current density, as reported in literature [30-32].

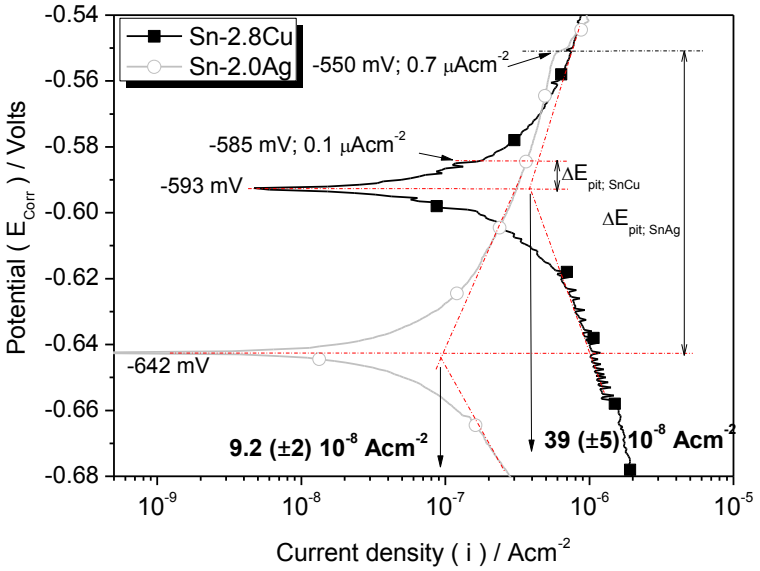

Figure 7. Experimental potentiodynamic polarization curves showing corrosion current density for both Sn-2%Ag and Sn-2.8%Cu solder alloys samples in a 0.5 M NaCl solution at 25 ^{o}C.

Considering the Sn-2%Ag alloy sample, a current density of about 9.2 (±2) 10^{-8} Acm^{-}2 (or 0.092 μAcm^{-2}) associated with a corrosion potential of -642 mV (SCE) is observed. The current density of the Sn-2.8%Cu alloy sample is considerably higher (of about four times, i.e. 39 (±5) 10^{-8} Acm^{-2} with -593 mV, SCE) than that of the Sn-Ag sample, as shown in Fig. 7. Although the observed cathodic reactions are similar for both Sn-Ag and Sn-Cu alloys, the Sn-Cu alloy sample exhibits a significant increase in the cathodic activity which is clearly observed in the cathodic branch of the Sn-Cu alloy sample.

By comparing the polarization plots, despite the noblest potential (-593 mV, SCE) which is exhibited by the Sn-Cu alloy sample, it has a higher corrosion current density, as aforementioned. Besides, the corresponding pitting potential (E_{pit}) of the Sn-Cu alloy sample is displaced of about 08 mV (*vs.*SCE) when compared with its E_{corr}.

Both the Sn-Ag and Sn-Cu samples present partial stabilization in the current density which start from ± 3 to 5 10^{-8}A cm^{-2}, as can be seen in Figs. 6 and 7. This seems to indicate corrosion of the Sn-rich phase, formation of tin oxide (Sn II oxide) and possibly initiation of mechanisms of precipitation and dissolution of a number of particles, e.g. $SnCl_2$, $Sn(OH)_4$, SnO, $SnCl^{-3}$ and $SnCl_6^{-2}$, as also reported in the literature [33-34]. Slight potential turbulences appear from -550 mV (SCE) and some potential breakdown occurs, which can be associated with pitting corrosion mechanisms.

Considering the difference between corrosion potential (E_{corr}) and pitting potential (E_{pit}) named as ΔE_{pit}, it can be seen that the Sn-Cu alloy has E_{pit} (-585 mV, SCE) very close to E_{corr} (-593 mV, SCE) resulting in a ΔE_{pit} of about 8 mV (SCE), as depicted in Fig. 7. On the other hand, the Sn-Ag alloy sample exhibit the highest ΔE_{pit} (± 92 mV, SCE), which corresponds to the difference between -642 mV (E_{corr}) and -550 mV (E_{pit}). Although these observations indicate that the Sn-Cu alloy has the corrosion potential displaced toward the nobler-potential side, it is more susceptible to pitting corrosion mechanisms and its corrosion current density is also higher when compared with that of the Sn-Ag alloy.

Besides, both the Sn-Ag and Sn-Cu alloy samples evidence primary passive current densities (i_{PP}) starting from -550mV (SCE) at 0.85 μAcm^{-2}, as shown in Fig. 6(b). Although the initial i_{PP} seems similar for both Sn-based alloys examined, the lowest and more stable i_{PP} is related to that of the Sn-Ag alloy, i.e. it is stable from about 1 μA cm^{-2} at -550mV (SCE) up to -455 mV (SCE) where a potential breakdown is evidenced, as shown in Fig. 6(b). On the other hand, the Sn-2.8%Cu alloy sample shows an i_{PP} also starting from about 0.85 μAcm^{-2} at -550 mV (SCE), however, evidencing a slight increase in i_{PP} up to ± 3 μAcm^{-2} at -432 mV (SCE). Thus, it can be concluded that the Sn-Ag alloy sample has a distinctly wider passive region with reduced passive current density associated with smaller trend to pitting corrosion.

The aforementioned observations, reinforce the corrosion resistance tendency observed previously with the results of EIS and impedance parameters (equivalent circuit), i.e., a better corrosion resistance being associated with the Sn-2%Ag alloy. However, it would be interesting to analyze the interconnection of the resulting corrosion behavior with the resulting microstructural arrangement, as a function of: solute content (difference between the corrosion potential of the phases forming the microstructure) and the morphology of the microstructure array which is intimately related to the cooling rate during the soldering process.

3.4 Microstructure and corrosion resistance

It is important to remark that similar Ag and Cu contents for the Sn-based alloys as well as a similar range of cooling rates have been selected for the present experimental study with a view to focusing on the evaluation of the effects of the corresponding microstructure arrays on the electrochemical corrosion behavior.

From the electrochemical point of view, since tin (Sn) has an anodic behavior with respect to silver (Ag), i.e. tin is more active (-500 mV, SCE) than Ag (-80 mV, SCE), a much larger anode area (more active, Sn) is expected to be present in the microstructure when compared with the

corresponding cathode area (nobler, Ag). When a Sn/Cu galvanic couple is considered, Sn again is anodic with respect to Cu, e.g. Cu (-220 mV, SCE) and Sn (-500 mV, SCE), which also induces to Sn anode reaction be normally proceeded.

From the metallurgical point of view, both the Sn-2%Ag and Sn-2.8%Cu alloys samples have the microstructures formed by a Sn-rich matrix and by Ag_3Sn and Cu_6Sn_5 intermetallics, respectively, as previously shown in Fig.2. Both samples were also extracted from the same position with respect to the casting cooled surface, i.e. a region characterized by a fine microstructural arrangement. The Sn-Ag alloy depicts a microstructure formed by a mixture of spheroids and fiber-like Ag_3Sn particles which are homogeneously distributed in the Sn-rich matrix. This Sn-rich matrix is constituted by fine and homogeneously distributed secondary dendrite arm spacings (λ_2 = 12 μm). The microstructure of the Sn-Cu alloy sample has also intermetallic particles (Cu_6Sn_5) with fine inter-branch spacings (λ) homogeneously distributed in the Sn-rich matrix. During solidification of the Sn-Ag alloy, the Sn-rich phase grows from the liquid in a non-faceted manner (growth with a rough interface), and the Ag_3Sn intermetallics grows cooperatively with the Sn-rich phase in the interdendritic region forming the eutectic mixture.

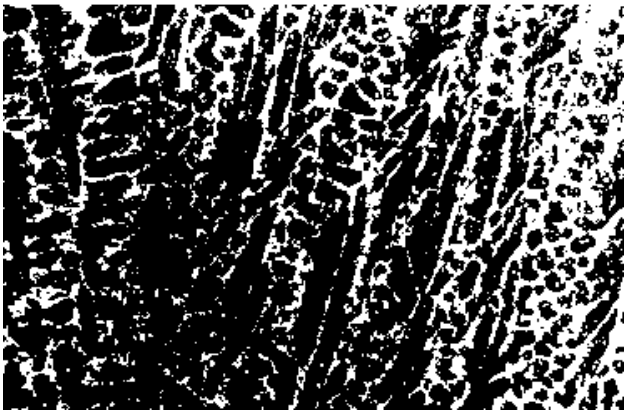

A White area is of about: 24.6 (±1.5) %

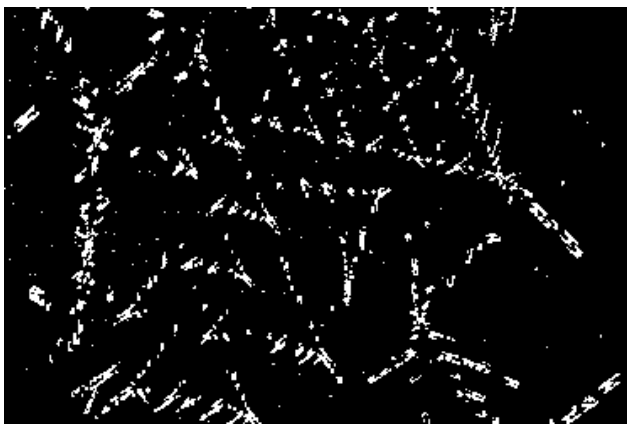

B White area is of about: 7.5 (±2) %

Figure 8. Binary micrographs of Sn-Ag **(a)** and Sn-Cu **(b)** solder alloys evidencing the ratio of anode/cathode: Sn-rich (matrix) and Ag_3Sn and Cu_6Sn_5 intermetallics.

On the other hand, considering the Sn-Cu alloy while the Sn-rich phase growth with a rough interface (non-faceted), the intermetallic Cu_6Sn_5 solidifies with interfaces that are smooth [16-17]. As a result, the boundaries between these two phases will not be perfectly conformed, but rather will be subjected to a certain strain, mainly on the Sn-rich phase side of the interface. It seems that these regions, because of such localized strain, could be more susceptible to the corrosion action than the intermetallic phase itself.

Besides, considering the discussion concerned the ratio anode/cathode areas of the Sn/Ag and Sn/Cu couples, which are determined by the resulting microstructure, it is clearly evidenced that the Sn-2%Ag alloy has a higher cathode area (Ag nobler area) when compared with that of the Sn-2.8%Cu alloy sample, as shown in Fig. 8. The micrographs depicted in Fig. 8 of both Sn-Ag and Sn-Cu alloys are shown in binary images (software ImageJ®) and the average percentages of the Sn-rich matrix (black) and Ag and Cu (white) regions were determined. Thus, the microstructure of the Sn-Ag alloy has of about 24.6 (±1.5) % of its surface formed by Ag-rich areas (cathode or nobler) while the Sn-Cu alloy has only 7.5 (±2) % corresponding to the cathode Cu-rich area.

With these observations, it can be concluded that the Sn-Ag microstructural arrangement has an important role on the electrochemical behavior, providing a better corrosion protection when compared with the results evidenced by the Sn-Cu alloy. This can be attributed to both the fine and homogeneously distributed spheroids and fiber-like Ag_3Sn intermetallic particles, and the decrease in the ratio of the anode/cathode area. The Ag_3Sn phase "envelops" the anode Sn-rich phase (dendritic matrix, active area) providing better pitting corrosion and decreasing the corrosion current density.

Differently the Sn-Cu alloy has fine inter-branch spacings associated with smaller Cu_6Sn_5 particles which provoke localized strains at the boundaries with the Sn-rich matrix, becoming considerably more susceptible to the corrosion action when compared to the Sn-Ag alloy. Besides, the ratio of the anode/cathode area is also higher (2.5 times) when compared to that of the Sn-Ag alloy, which favored the better electrochemical behavior of the Sn-Ag alloy.

These present experimental electrochemical results, related to tests carried out in a sodium chloride solution at room temperature, can be useful to demonstrate the potential reliability of both binary Sn-Ag and Sn-Cu solder alloys.

Table 2. Average prices and relative costs for commercially pure materials and SnAg and SnCu solder alloys [1, 35].

Material	Average Cost ($US/ kg)	Relative Cost
Tin (Sn)	7~9	1.8
Silver (Ag)	150~250	31
Copper (Cu)	2~7	0.8
Lead (Pb)	1~3	0.3
Sn40Pb	5~8*	1
Sn2Ag	10~14*	1.8
Sn2.8Cu	7~9*	1.2

(*) Values estimated from the individual prices of metals composing the alloy

Table 2 shows ranges of the average prices (U.S. dollars per kilogram) in order to permit relative costs of the some solder materials with respect to the traditional Sn40Pb solder alloy to be established. The pricing information has been collected from the literature [1, 35]. Considering that the metals prices can vary significantly over time and with the way it is processed or treated, a relative cost index has been composed. This index was based on that of the traditional Sn40Pb solder alloy and represents the average material price per kilogram divided by the corresponding price of the Sn40Pb alloy (i.e. US$ 6.5/kg). It can be seen that the Sn-2Ag and Sn-2.8Cu alloys have relative cost indices of 1.8 and 1.2, respectively.

From the metallurgical point of view, it is known that the melting point of Ag (961 ^{o}C) and Cu (1084 ^{o}C) are relatively higher than that of Sn (232 ^{o}C). However, in order to elaborate both Sn-Ag and Sn-Cu alloys, Ag and Cu in powder form can be dissolved into the molten Sn. Once elaborated in plates or bars, a same level of electric energy consumption is spent with these two alloys in the soldering process.

Although the Sn-2Ag alloy has an index cost of about 1.5 (50% higher than the Sn-2.8Cu alloy), it can also be clearly observed that its corresponding electrochemical corrosion behavior is considerably better: the polarization resistance is of 1.5 higher ($\pm$ 39 kΩ cm^2 for the SnAg alloy against $\pm$ 26 kΩ cm^2 for the SnCu alloy) and a corrosion current density of about 4 times lower ($\pm$ 9 μAcm^{-2} against $\pm$ 39 μAcm^{-2}, respectively). Based on these observations, it can be said that a trade-off between the production cost (mainly guided by Silver price) and the resulting electrochemical corrosion behavior can be considered for the selection of an appropriate solder alloy.

4. CONCLUSIONS

Based on the present experimental corrosion tests carried out with both Sn-2Ag and Sn-2.8Cu alloys, it can be concluded that the electrochemical corrosion behavior is intimately associated with both metallurgical and electrochemical aspects. In this context, it can be concluded that a microstructure of a Sn-2Ag solder alloy characterized by a fine dendritic array associated with fine and homogeneously distributed Ag_3Sn intermetallic particles has proved to have a better electrochemical corrosion behavior when compared with that of a microstructure of a Sn-2.8Cu solder alloy formed by fine and homogeneously distributed Cu_6Sn_5 intermetallics in the Sn-rich matrix.

From the impedance parameters, it can be said that both Sn-Ag and Sn-Cu solder alloys samples have similar capacitances Z_{CPE1}, which indicate similar corrosion mechanisms, however, their corresponding polarization resistances, which represent the metallic corrosion and polarization resistances of adsorbed intermediates, are considerably different. This can be attributed to the different growth forms of the Sn-rich phase (non-faceted) and the intermetallics (faceted) in the case of the Sn-Cu solder alloy, which can induce a certain strain in the atomic level along the boundaries between these phases. As a consequence of these localized strains, regions more susceptible to corrosion action are produced. Furthermore, its fine microstructure array has also proved to provide more accentuated pitting corrosion due to the higher number of galvanic couples that are formed. On the other hand, the microstructure of the Sn-Ag alloy having a fine secondary dendrite spacing with Ag_3Sn intermetallic

particles homogeneously distributed in the interdendritic region, was shown to favor the corrosion resistance since the nobler phase "envelops" the more active Sn-rich areas decreasing the degradation. This can be seen analyzing the polarization results, which show that the Sn-2Ag alloy sample has a higher resistance to pitting formation, a more stable passivity and lower corrosion current density than the Sn-2.8Cu alloy sample. Besides, from the economical point of view, considering both the relative cost and the electrochemical behavior, it can be said that a trade-off between the production cost (mainly guided by Silver price) and the resulting electrochemical corrosion behavior can be considered for the selection of an appropriate solder alloy

ACKNOWLEDGEMENTS
The authors acknowledge the financial support provided by FAPESP (The Scientific Research Foundation of the State of São Paulo, Brazil), and CNPq (The Brazilian Research Council).

References

1. M. Abtew, G. Selvaduray, *Mater. Sci. Eng*. 27 (2000)95
2. W.H. Muller, *Microelectronics Reliability* 44 (2004)1901
3. J. Shen, Y.C. Chan, S.Y. Liu, *Intermetallics* 16 (2008)1142
4. L.R. Garcia, W.R. Osório, L.C. Peixoto, A. Garcia, *Materia- Rio de Janeiro* 14 (2009)767.
5. L.R. Garcia, W.R. Osório, L.C. Peixoto, A. Garcia, *Mater. Charact*. 61 (2010) 212.
6. K. Nogita, *Intermetallics* 18 (2010) 145.
7. D. Li, P.P. Conway, C. Liu, *Corros. Sci*. 50 (2008) 995.
8. F. Song, S.W.R. Lee, Electr. *Components and Technology Conference* (2006) 891-898.
9. L.R. Garcia, W.R. Osório, A. Garcia, *Mater. Design* 32 (2011) 3008
10. W.R. Osório, L.R. Garcia, L.C. Peixoto, A. Garcia, *Mater. Design* 32 (2011) 4763
11. J. Shen, Y.C. Liu, Y.J. Han, H.X. Gao, C.Wei, Y.Q. Yang, *Trans. Nonferrous Met. Soc. China* 16 (2006)59
12. F. Ochoa, J.J. Williams, N. Chawla, *J. Electron. Mater*. 32 (2003)1414
13. G. Li, Y. Shi, H. Hao, Z. Xia, Y. Lei, F. Guo, *J. Alloys Compd*. 491 (2010)382.
14. W.R. Osório, J.E. Spinelli, C.R.M. Afonso, L.C. Peixoto, A. Garcia, *Electrochim. Acta* 56 (2011) 8891
15. F. Song, S.W.R. Lee, *Electr. Components and Technology Conference* (2006) 891-898.
16. J. Machida, *J. Japan Inst. Metals* 70 (2006) 7073.
17. R.K. Chinnam, C. Fauteux, J. Neuenschwander, J. Janczak-Rusch, *Acta Mater*. 59 (2011) 1474.
18. X. Liu, M. Huang, Y. Zhao, C.M.L. Wu, L. Wang, *J. Alloys Compounds* 492 (2010)433
19. K.S. Kim, S.H. Huh, K. Suganuma, *J. Mater. Sci. Eng*. A333 (2002) 106.
20. N. Tamura, R. Ohshita, M. Fujimoto, S. Fujitani, M. Kamino, I. Yonezu, *J. Power Sources* 107 (2002) 48.
21. J. Shen, Y. Liu, H. Gao, *J. Univers. Scie. Technol. Beijing* Z3 (2006) 333.
22. J.E.G. Gonzalez, J.C. Mirza-Rosca, *J. Electroanal. Chem*. 471 (1999) 109.
23. W.R. Osório, N. Cheung, L.C. Peixoto, A. Garcia, *Int. J. Electrochem. Sci*., 4 (2009) 820
24. J.A. Ruiz, I. Rosales, J.G. Gonzalez-Rodriguez,J. Uruchurtu, *Int. J. Electrochem. Sci*., 5 (2010) 593
25. W.R. Osório, L.C. Peixoto, M.V. Canté, A. Garcia, *Electrochim. Acta* 55 (2010) 4078.
26. W.R. Osório, L.C. Peixoto, A. Garcia, *Mater. Corros*. 61 (2010) 407.
27. I.E. Castañeda, J.G. Gonzalez-Rodriguez, G. Dominguez-Patiño, R. Sandoval-Jabalera, M.A.Neri-Flores, JG. Chacon-Nava, A. Martinez-Villafañe, *Int. J. Electrochem. Sci.*, 6 (2011) 404

28. H .A. Barham, S. A. Brahim, Y. Rozita, K. A. Mohamed, *Int. J. Electrochem. Sci.*, 6 (2011) 181
29. W.R. Osório, L.C. Peixoto, A. Garcia, *Int. J. Electrochem. Sci*. 6 (2011) 1522.
30. W.R. Osório, D.J. Moutinho, L.C. Peixoto, I.L. Ferreira, A. Garcia, *Electrochim. Acta* 56 (2011) 8412
31. W.R. Osório, D.M. Rosa, A. Garcia, *Electrochim. Acta* 56 (2011) 8457
32. W.R. Osório, L.C. Peixoto, D.J. Moutinho, L.G. Gomes, I.L. Ferreira, A. Garcia, *Mater. Design* 32 (2011) 3832
33. X.L. Zhang, Zh.H. Jiang, Zh.P Yao, Y. Song, Zh.D. Wu, *Corros. Sci*. 51 (2009) 581.
34. D. Li, P.P. Conway, C. Liu, *Corros. Sci.* 50 (2008)995.
35. Carol Handwerker, "NCMS Lead Free Solder Project: A National Program", NEMI Lead Free Solder Meeting, Chicago, May 25, 1999